Characterization of the effect of intake air swirl motion on time-resolved in-cylinder flow field using quadruple proper orthogonal decomposition

Hanyang Zhuang [a], David L.S. Hung [a,b,*]

[a] University of Michigan-Shanghai Jiao Tong University Joint Institute, Shanghai Jiao Tong University, Shanghai, China
[b] School of Mechanical Engineering, Shanghai Jiao Tong University, National Engineering Laboratory for Automotive Electronic Control Technology, Shanghai, China

ARTICLE INFO

ABSTRACT

The control of intake air swirl motion is often used in spark-ignition direct-injection (SIDI) engine to improve its in-cylinder fuel–air mixing process especially under engine idle and low load conditions. In this experimental investigation, a novel technique combining the time-resolved particle image velocimetry (PIV) with quadruple proper orthogonal decomposition (POD) is implemented to analyze the time-resolved in-cylinder velocity measurements in an optically-accessible SIDI engine. The intake air swirl motion is introduced into the engine cylinder by a control valve installed in one of two air intake ports. Experimental results show that a strong linear correlation exists between the intake flow swirl ratio and vorticity flow field in the cylinder. This correlation ensures high data reliability of swirl motion control and provides a novel basis to directly compare the flow field measurements under different swirl ratio conditions. The quadruple proper orthogonal decomposition analysis is then applied to the velocity flow fields to separate the highly dynamic in-cylinder flow characteristics into four distinct categories: (1) dominant flow structure; (2) coherent structure; (3) turbulent structure; and (4) noise structure. The results show that the dominant flow structure varies strongly with swirl ratio, and its kinetic energy is also directly related to the swirl ratio. The coherent structure captures the large scale flow characteristics, but its kinetic energy is much lower and exhibits larger cycle-to-cycle variations. The turbulent structure contains similar level of kinetic energy at different swirl ratios but without much cycle-to-cycle variation. Finally, the noise structure contains very low kinetic energy which only alters the dynamic nature of the flow field slightly. In summary, the effect of swirl ratio on in-cylinder flow field is mostly captured by the dominant flow structure and partially captured by the coherent flow structure. The turbulent flow structure can characterize the high-order flow variation. The noise structure can be neglected due to the low energy captured.

1. Introduction

Automobiles are constantly being improved with the implementation of innovative techniques and features to meet the requirements of higher fuel efficiency and lower engine emissions. Within the last few decades, internal combustion engines have been significantly improved in numerous ways, including the adoption of variable valve actuation (VVA), multi-stage turbocharging, and spark-ignition direct-injection (SIDI). Since the legislation of emission control is becoming more rigorous, downsized engines with high output power are becoming the trend for automobiles. For instance, smaller boosted SIDI engines have

demonstrated high potential for emission reduction and improved engine performance [1]. However, the drawbacks of SIDI technology are short fuel vaporization time and over-penetration of liquid fuel in the cylinder. Specifically, insufficient fuel vaporization time leads to inhomogeneity of fuel distribution and large droplets before the spark ignition takes place, which causes slow, or incomplete combustion, with excess hydrocarbon (HC) emissions. Likewise, excessive penetration of fuel spray under higher injection pressure leads to fuel impingement and undesirable wall wetting – the main reasons for lubrication oil dilution and high HC and soot emission. Considerable research has been carried out to resolve the issue by the improvement of SIDI spray systems and injector characteristics [2,3]. The other approach to enhance the vaporization process is to utilize the full potential of the in-cylinder flow field characteristics. Enhancing in-cylinder flow field is considered to be another key method for optimal spray development and rapid

---

flame propagation which would significantly improve engine performance. The two dominant in-cylinder flow processes – namely, tumble flow and swirl flow – have been studied for decades by numerous researchers [4–7]. In addition to the flow introduced by charge motion, the motions of engine piston and exhaust valve [8], and flow pulsation [9], are also considered to be critical factors influencing the in-cylinder flow characteristics. With the development of high-speed particle image velocimetry (PIV), temporally resolved in-cylinder flow field measurements can be obtained at various crank angle degrees (CAD), and over multiple engine cycles. Taking the benefits of high-speed PIV, researchers are able to study the averaged flow field of multiple cycles, and at the same time investigate the strong cycle-to-cycle variation characteristics of in-cylinder flow. For this reason, extensive researches have been performed to directly analyze the in-cylinder processes of individual cycles [7], or use statistical methods to obtain representative flow field features from multiple cycles [10–12]. As a result, both ensemble-averaged flow data and time-varying sets of velocity flow field results can be analyzed using these more complex methods.

One particular method to resolve the ensemble average and variation properties simultaneously is the proper orthogonal decomposition (POD), which has been widely used to study the fluctuations of air flow in internal combustion engines. POD was first introduced to study large scale eddies in turbulent flows [13], and it was further developed for flow analysis by separating the turbulent fluctuations and unsteady swirl motion [14]. Since this statistical technique was applicable to extract the engine flow characteristics, further research had been implemented by implementing POD to analyze the spray and combustion processes [15–18]. It is widely accepted that appropriate enhancements of fuel atomization and mixing depend on the understanding of in-cylinder flow fields obtained from PIV experiments. Therefore, POD technique is a powerful tool for providing quantitative information on engine flow fields [19,20]. For example, Druault et al. made a POD analysis of PIV data to understand the variability change during an engine cycle [21]. Vu and Guibert focused on variations inside the engine occurring with modification of the inlet pipe [22]. Grafieaux et al. [14] and Zhuang et al. [23] introduced POD into vortex analysis to study the flow field characteristics in motoring optical engines. The application of POD also provides an insightful approach to compare the results between experimental PIV data and large eddy simulation (LES) results. For instance, Qin et al. [24] and Abraham et al. [25] made comprehensive analysis of the comparison between numerical LES results and experimental PIV data. However, the POD technique described above only focused on a fixed crank angle degree to reveal the corresponding cycle-to-cycle variations. Therefore, some researchers extended the POD technique into so-called "phase-invariant POD" to resolve the temporal properties of transient flow fields [26–28]. Further development of POD is to classify the POD modes into several groups according to their special behavior. This idea was first proposed in the study of engine flow field variations by Roudnitzky et al. [29]. They partitioned the flow fields into three compositions (triple decomposition) based on an energy criterion. Then, Qin et al. [24,30] expanded the application and decomposed the engine flow fields and spray images into four different parts (quadruple decomposition) to further describe the in-cylinder phenomena.

This paper focuses on characterizing the effect of intake charge swirl motion on the transient behavior of in-cylinder flow field using the quadruple POD analysis. This investigation demonstrates a first attempt to reveal the impact of intake swirl ratio (SR) on in-cylinder engine flow using the quadruple POD analysis technique. The concept is derived by reconstructing classical POD modes of similar features into several groups to better represent the flow field properties [22,24,29]. In a classical POD analysis, the first

mode usually contains the dominant flow characteristic; then the remaining higher modes only show limited differences in kinetic energy among each other, which has led to an imprecise determination of the properties of individual mode. However, with the utilization of quadruple POD, the reconstructed groups from individual classical POD modes can represent more significant flow field characteristics. In this paper, flow fields are divided into four main structures, based on a criterion stated in the Data Processing Techniques section: dominant structure, coherent structure, turbulent structure, and noise structure. This decomposition is applied to five sets of time-resolved flow field data under various intake swirl ratios. The results show that the characteristics of the flow strongly depend on the swirl ratio and crank angle.

In the following sections, the experimental setup is introduced first, followed by the algorithm section to explain the classical and quadruple POD techniques. In the results and analysis section, the comparisons between swirl ratio measured on flow bench and vorticity measured by PIV, are shown first. Next, the flow characteristics are depicted and analyzed to reveal mean and variable features of the dominant, coherent, and turbulent structures reconstructed through quadruple POD. Finally, conclusions are drawn according to the results to highlight the benefits of this novel POD analysis technique.

2. Experimental setup

The experiment was carried out in an optically accessible single-cylinder SIDI engine (Fig. 1). The design was based on a four-valve SIDI production engine with a bore of 86 mm, stroke of 94.6 mm, connecting rod length of 160 mm, and the compression ratio of 8.8. As shown in Fig. 1a, the engine was equipped with an optical liner providing full access to the interior of engine cylinder; it also allowed laser illumination into the cylinder for PIV measurements. The intake swirl control valve was installed in one of the two intake ports (Fig. 1b). The intake port without the control valve was named the 'primary intake port'; the one with
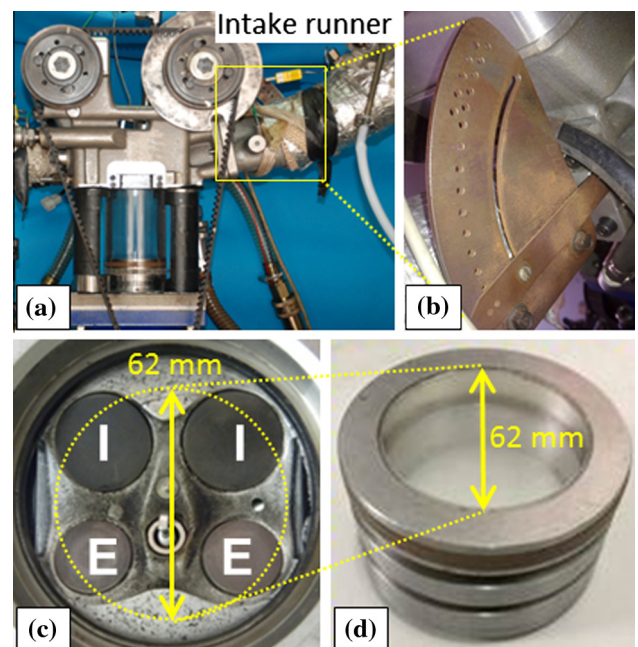

Fig. 1. (a) Optical engine overview with swirl control valve shown in box (valve located at the opposite side of the photographer); (b) intake air swirl control valve; (c) cylinder head configuration (dotted circle indicates viewable area from piston); (d) quartz optical piston.

the control valve was called the 'secondary intake port'. A detailed explanation of the function of swirl control valve is provided later. The engine cylinder head was configured with two intake valves and two exhaust valves. The fuel injector and spark plug were located in the center of cylinder head, with the injector near the intake ports and the spark plug near the exhaust ports. The dotted line in Fig. 1c indicates the viewable area when the piston was at the focal plane, which was set at 30 mm below the injector tip in this engine. The corresponding optical piston, with a 62 mm-diameter quartz inserted, was depicted in Fig. 1d.

As depicted in Fig. 2, the crank angle resolved PIV experiment was implemented along the swirl plane which was parallel to the plane of the piston top. The selection of the focal plane at 30 mm below the injector tip was chosen to fully realize the impact of intake flow on spray, based on prior experimental findings. The optical engine was motored by an AVL dyno at 800 rpm while the high-speed imaging system operated at 2400 Hz to capture a pair of images per two crank angle degrees. The double-pulse PIV laser (Nd:YLF PIV laser at 527 nm, Litron) was synchronized with the high-speed camera (Phantom V7.3, Vision Research) to record a pair of particle images at 10 μs apart. Post processing was then applied to calculate the flow field based on the particle image pair.

Primary and secondary intake ports are also depicted in Fig. 2. The cross section image on the right shows the view from the camera. The dotted circle represents a 62 mm-diameter viewable area, when the piston was at the focal plane. The primary intake port is always open and the secondary intake port is closed partially or completely based on the swirl motion control valve position. If the secondary intake port is closed, intake air enters the cylinder only from the primary intake port, which creates a clockwise swirl air motion viewed from the 45° mirror. When the secondary intake port is open, intake air could enter the cylinder from both intake ports, generating a reduced swirl motion. This paper focuses on the effect of intake air swirl ratio on in-cylinder flow features, where five different swirl ratio conditions are taken into consideration rather than only the highest and lowest swirl ratio.

Fig. 3 shows the structure of the intake swirl motion control valve. There are 20 preset positions for the swirl ratio adjustments. The in-cylinder flow swirl ratio has been measured on a cylinder head flow bench. The highest swirl ratio is 5.68 and the lowest is 0.55. To show the significant distinctions, five swirl valve positions,
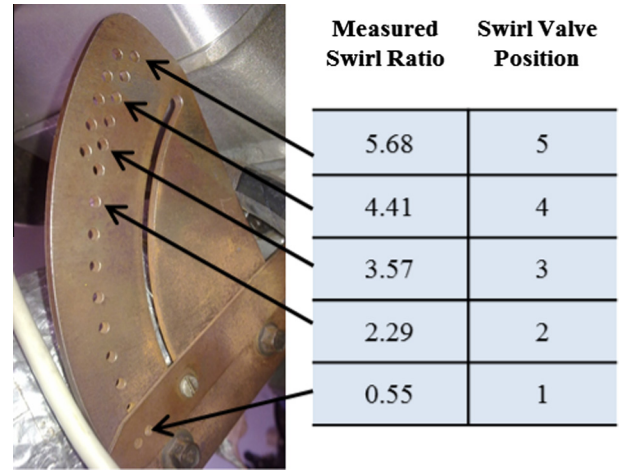

Measured Swirl Ratio	Swirl Valve Position
5.68	5
4.41	4
3.57	3
2.29	2
0.55	1

Fig. 3. Swirl control valve and measured swirl ratio with corresponding valve positions.

with a step of about one swirl ratio difference, were chosen. With this setup, the impact of intake swirl ratio on in-cylinder flow can be resolved and analyzed more efficiently.

3. Data processing techniques

3.1. Proper orthogonal decomposition (POD)

Proper orthogonal decomposition is a mathematical technique used to resolve a data set based on its statistical behaviors. In this section, the principle of POD is provided, whereas the extension of POD (the quadruple POD) is presented next. To clarify the differences between the two POD techniques, POD (called "classical POD" in this paper), is explained in this section; the next section will address the quadruple POD. While the POD technique as a mathematical method has been studied and used for a long time, the application of POD in flow field analysis does not have a long history. References regarding the application and introduction of
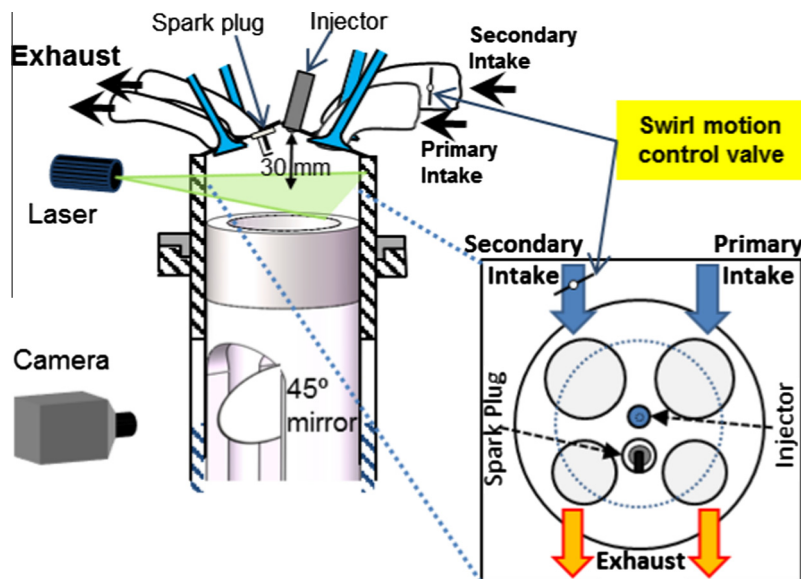

Fig. 2. Setup of PIV experiment with view of swirl plane and location of swirl motion control valve.

POD are provided with a MATLAB script included [31,32]. The POD technique is applicable to any scalar field, such as combustion flame and luminosity, or a vector field, like air flow field. The following explanation of the POD principle is based on an example of a scalar field.

POD is an empirical method, therefore the decomposition results are unique and dependent upon the input dataset. The input data are called 'snapshots' here, while the collection of all snapshots is indicated by a matrix $s_{(i,j)}^{(k)}$. The superscript index $k = 1, 2, \ldots, K$ means the kth snapshot, and there are totally K snapshots in the input dataset. Meanwhile, all snapshots must have the same size. Parameters i and j stand for the pixel numbers of row and column for each snapshot, respectively. Then the set of POD modes based on the input dataset is defined as $\varphi_{m(i,j)}, m = 1, 2, \ldots M$, and the corresponding coefficients of mth mode to the kth snapshot are indicated by $c_m^{(k)}$. These modes are orthonormal, meaning that they are orthogonal to each other, and the magnitude of each mode is equal to unity. The number of modes and snapshots are maintained to be identical in most application areas. The next section introduces the properties of snapshots, modes, and coefficients, followed by an explanation of the procedure to obtain the modes and coefficients.

According to Eq. (1), the relationship of the modes and coefficients to the snapshots can be described as:

$$s^{(k)} = \sum_{m=1}^{M} c_m^{(k)} \varphi_m. \tag{1}$$

The coefficients multiplying the modes in the matrix way reconstruct back the original input snapshots. In addition, the modes and coefficients must satisfy Eq. (2) to represent the modes properties:

$$\sum_{k=1}^{K} \left\| s^{(k)} - \sum_{m=1}^{N} c_m^{(k)} \varphi_m \right\|^2 \to \min. \tag{2}$$

where $\| \cdot \|$ denotes the L^2 norm and N in the summation operator indicates any arbitrary integer from 1 to M. This means for any first N modes, Eq. (2) will always stand. This property allows the POD modes to capture the most dominant characteristics of the input dataset.

For the given K snapshots with size of $I \times J$, the first step is to reshape the $I \times J$ matrix of the snapshot into a vector with dimension of 1 row and $(I \times J)$ columns. The matrix R indicating the collection of all snapshots, is obtained by combining all row vectors together according to:

$$R = \begin{bmatrix} s_{i=1\,j=1}^{(1)} & s_{i=1\,j=2}^{(1)} & \cdots & s_{i=1\,j=J}^{(1)} & s_{i=2\,j=1}^{(1)} & \cdots & s_{i=I\,j=J}^{(1)} \\ s_{i=1\,j=1}^{(2)} & s_{i=1\,j=2}^{(2)} & \cdots & s_{i=1\,j=J}^{(2)} & s_{i=2\,j=1}^{(2)} & \cdots & s_{i=I\,j=J}^{(2)} \\ \vdots & \vdots & \vdots & \vdots & \vdots & \vdots & \vdots \\ s_{i=1\,j=1}^{(K)} & s_{i=1\,j=2}^{(K)} & \cdots & s_{i=1\,j=J}^{(K)} & s_{i=2\,j=1}^{(K)} & \cdots & s_{i=I\,j=J}^{(K)} \end{bmatrix}, \tag{3}$$

Then the spatial correlation matrix C is calculated through the cross product of the scalar field matrix R:

$$C = \frac{1}{K} R R^T. \tag{4}$$

Next, the eigenvalues $(\lambda_m, m = 1, 2, \ldots, M)$ and eigenvectors $(\bar{\beta}_m, m = 1, 2, \ldots, M)$ of the correlation matrix C are generated by solving the following eigenvalue problem:

$$C \bar{\beta}_m = \lambda_m \bar{\beta}_m. \tag{5}$$

Finally, the POD modes (φ_m), are derived by projecting the snapshot matrix R onto the eigenvectors $(\bar{\beta}_m)$ obtained by Eq. (5). Meanwhile, the coefficients $c_m^{(k)}$ can be obtained by projecting the

snapshot matrix R on the POD modes (φ_m). Because the POD modes are orthonormal, they do not contain the magnitude information. The magnitude of each mode is expressed through the corresponding coefficients. Moreover, the energy (which represents the sum of the square of pixel intensity for scalar snapshots, or the kinetic energy for the velocity vector snapshots), of the mth mode is calculated using Eq. (6):

$$E_m = \frac{1}{2} \sum_{k=1}^{K} \left(c_m^{(k)} \right)^2. \tag{6}$$

3.2. Quadruple POD

The POD analysis method in previous paragraphs is a classical approach. However, researchers have found that individual POD modes may not provide enough detail information to capture the dominant and fluctuating structures of an input data set such as the in-cylinder flow field. In order to improve POD analysis, a quadruple POD method has been developed by previous researchers [24,29]. The first step of the quadruple POD is to decompose the input flow fields to obtain all POD modes using the classical POD method. Based on the relevance index (R_p) analysis which will be explained next, the modes are then classified into four different structures: dominant structure, coherent structure, turbulent structure, and noise structure. Each of the structures represents a specific characteristic of the original flow, and the kinetic energy captured by each structure reflects the significance of that structure in the flow.

To obtain the POD modes, it is necessary to utilize the classical POD analysis. In this paper, there are 100 snapshots of the in-cylinder flow field at a certain test condition; therefore 100 modes are generated after applying the classical POD and illustrated in the top schematic of Fig. 4. To carry out the quadruple POD analysis and classify the modes, an algorithm based on the relevance index is applied to the 100 modes. The relevance index is calculated according to Eq. (7):

$$R_p(u, v) = \frac{u_1' v_1 + u_2' v_2}{\sqrt{u_1' u_1 + u_2' u_2} \sqrt{v_1' v_1 + v_2' v_2}}, \tag{7}$$

where u_1 and u_2 indicate the x-direction velocity in flow field #1 and #2, and v_1 and v_2 indicate the y-direction velocity of the same flow field. u and v are column vectors, including all flow field velocities (A detailed explanation of the form of flow field can be found in [32]). The relevance index indicates the quantitative similarity between two flow fields, and its value ranges between -1 and 1. A relevance index of 0 means that the two input flow fields are orthogonal (i.e., no similarity) to each other. A relevance index of 1 indicates that the two flow fields are identical to each other, and the closer to 1 the index is, the more similar the two flow fields are. On the contrary, an index of -1 means the two flow fields are exactly in opposite direction, while an index approaching -1 shows the flow fields are more similar in an opposite direction. In addition, if two flow fields are either identical or opposite to each other, they can be represented by following relationship:

$$u_1 = N u_2 \quad \text{and} \quad v_1 = N v_2, \tag{8}$$

where u_1, u_2 and v_1, v_2 are x-direction and y-direction components of two flow fields, respectively; N is a non-zero rational number same for both components; when N is positive, the two flow fields are identical; when N is negative, the flow fields are opposite.

The first POD mode usually contains the most significant characteristic of input flow fields by capturing more than half of the kinetic energy. In addition, the first mode is similar to the ensemble average of the snapshots shown in previous study [18], so the first mode itself is considered as the dominant structure of the
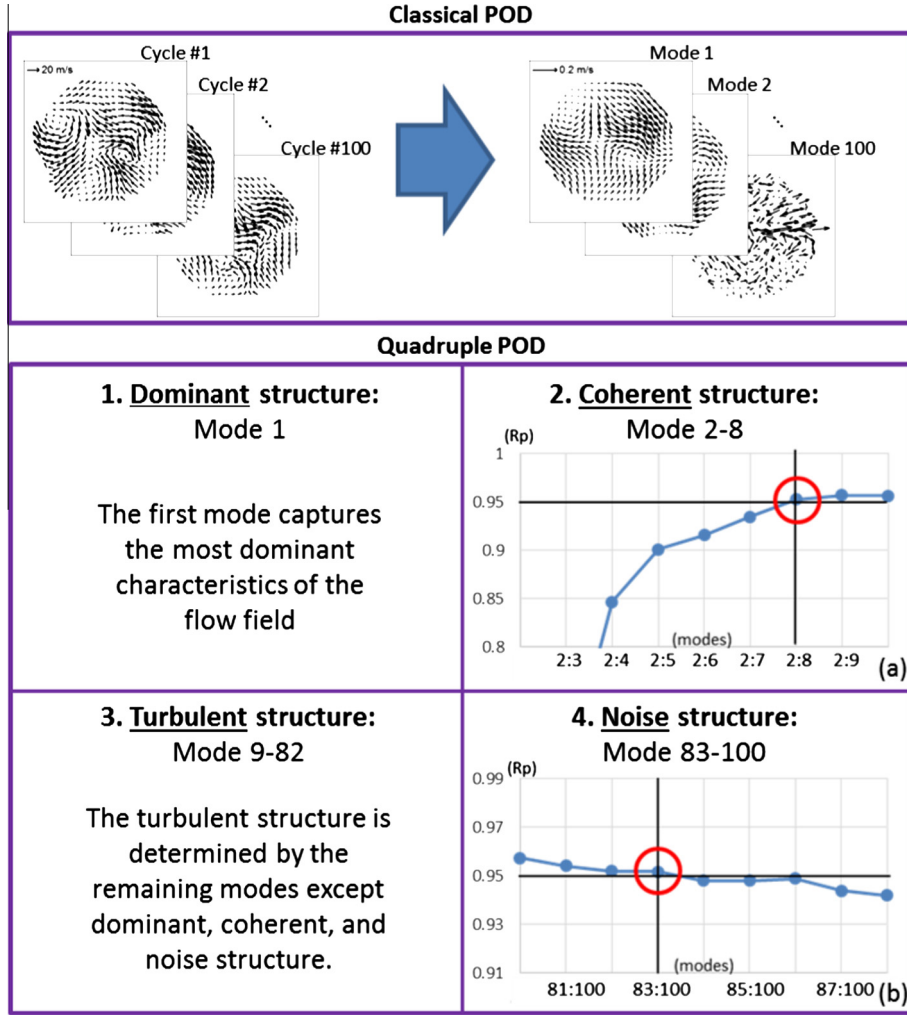
Fig. 4. Classical POD and quadruple POD analysis procedures and four structures obtained by quadruple POD at −280 CAD and swirl ratio of 5.68. (a) Relevance index evolution for reconstruction of coherent structure; (b) relevance index evolution for reconstruction of noise structure.

flow. After the dominant structure has been determined, the next step to obtain the coherent structure starts by temporally removing the first mode from the dataset. Since the ensemble average has already been captured by the dominant structure, the coherent structure captures the second significant properties characterizing the large-scale flow. Before determining the coherent structure, the definition of reconstructed structure (denoted by $H_{a:b}^{(k)}$), is stated as Eq. (9):

$$H_{a:b}^{(k)} = c_a^{(k)} \boldsymbol{\varphi}_a + c_{a+1}^{(k)} \boldsymbol{\varphi}_{a+1} + \cdots + c_b^{(k)} \boldsymbol{\varphi}_b, \tag{9}$$

where a and b are integer indices of the classical POD modes, with $a, b \in [1, 100]$, and $a \leqslant b$. $c_a^{(k)}$ is the corresponding coefficient of ath mode to the kth snapshot. $\boldsymbol{\varphi}_a$ represents the ath mode obtained by classical POD. The reconstructed structure is a linear combination of several POD modes of a certain snapshot; therefore k can be any arbitrary number from 1 to 100 in this study. However, quadruple POD treats each cycle individually, so cycle number k must be assigned to a certain number between 1 and 100.

For the remaining modes from mode 2 to mode 100, the following procedures will be applied to determine the coherent structure: First, the relevance index between mode 2 multiplying its coefficients ($c_2^{(k)} \boldsymbol{\varphi}_2$, which is represented by $H_{2:2}^{(k)}$ according to Eq. (9)), and the sum of mode 2 and 3 by respectively multiplying

their corresponding coefficients ($c_2^{(k)} \boldsymbol{\varphi}_2 + c_3^{(k)} \boldsymbol{\varphi}_3$, denoted by $H_{2:3}^{(k)}$), is calculated as follows:

$$I_{2:3}^{(k)} = R_p \left(H_{2:2}^{(k)}, H_{2:3}^{(k)} \right). \tag{10}$$

The reconstructed structure of modes 2 and 3 (i.e., $H_{2:3}^{(k)}$) captures more general flow characteristics than either mode 2 or mode 3 alone. Next, the relevance index of the reconstructed structure of modes 2+3 ($H_{2:3}^{(k)}$), with the reconstructed structure of modes 2+3+4 ($H_{2:4}^{(k)}$), is calculated to be $I_{2:4}^{(k)}$. It can be concluded that in each iteration, the previous reconstructed structure ($H_{2:N}^{(k)}$), where N is an arbitrary integer (from 3 to 99 in this case), is correlated with the reconstructed structure of one more mode ($H_{2:N+1}^{(k)}$). Then the iteration continues until the relevance index value ($I_{2:N+1}^{(k)}$) exceeds a value of 0.95, which is usually considered a very high level of similarity existing between two reconstructed flow fields [24,30]. The above process is depicted in the Fig. 4a. When the relevance index of $I_{2:8}^{(k)}$ is over 0.95, this reconstructed structure $H_{2:8}^{(k)}$ is capable of capturing the large-scale coherent flow characteristics of the input flow field.

The next step of quadruple POD technique is to decide the mode numbers to reconstruct the noise structure, then the rest of the

modes are reconstructed to be the turbulent structure. In a manner similar to the previous process, this is accomplished by starting from the last mode (the 100th mode) and adding the preceding mode (the 99th mode) into the summation for the relevance index calculation. For example, the first iteration is to correlate mode 100 with the reconstructed structure of mode 99 + 100 ($c_{99}^{(k)}\varphi_{99} + c_{100}^{(k)}\varphi_{100}$, denoted by $H_{99:100}^{(k)}$). Then the next step becomes 99:100 correlating with 98:100, etc. The iteration continues until the relevance index exceeds 0.95, as shown in Fig. 4b. Illustrated in this example, the noise structure is reconstructed by using mode 83 to mode 100.

Finally, the turbulent structure is reconstructed using the remaining modes, without those already used for constructing the dominant, coherent, and noise structures. As depicted in Fig. 4, the dominant flow is the first mode which represents the most dominant averaged flow characteristics. The coherent structure is reconstructed through mode 2–mode 8, which represents the large-scale coherent flow structure. The turbulent structure is obtained by all the modes from 9 to 82, which indicates the small-scale fluctuating turbulence part of the flow field. Finally, the noise structure consists of the modes from 83 to 100 and it represents the high-order noise introduced through experiments and data processing.

4. Results and analysis

The swirl motion in engine plays an important role in enhancing fuel–air mixing and flame propagation, especially under engine idle conditions where the air charge motion is weak. This is the main reason why a swirl motion control valve is introduced. Due to the significant effect of swirl motion in the engine cylinder on the fuel–air mixing and combustion processes, it is important to understand the in-cylinder flow field characteristics from the PIV experiment, since the velocity images and the derived vorticity images can be intuitively used for observation and quantification of in-cylinder flow properties.

Fig. 5 illustrates the ensemble average of the flow fields (shown as vectors in the figure), of 100 cycles and the corresponding vorticity magnitude (shown as background scalars field in the figure), at two selected crank angles during intake stroke (−280 CAD ATDC), and compression stroke (−120 CAD ATDC), at five different swirl ratio values. Blue area represents flow rotating in the

clockwise direction; red area represents a counter-clockwise rotating flow. Significant differences can be found between these two crank angles, while only minor changes are observed within one crank angle between adjacent flow fields under the effect of swirl motion. At intake stroke of −280 CAD ATDC, both clockwise and counter-clockwise vortices exist with much stronger vorticity strength compared to the second row. However, at −280 CAD, no strong swirl structure appears, and the vortices in different directions interact with each other, causing the spatial variations observed at −280 CAD ATDC. Meanwhile, the strength of small vortices is stronger under higher swirl conditions than lower swirl conditions. This trend is affected by different levels of intake air charge velocity. However, at −120 CAD ATDC, the in-cylinder flow fields act as a single coherent large-scale vortex for each condition. These uniform vorticity distributions indicate that after the interaction during intake stroke, the flow field eventually forms a highly regulated swirl motion in the compression stroke.

After observing the flow field under various swirl ratio values, average vorticity is obtained using the flow field results to indicate swirl motion strength. When the average vorticity approaches zero, it means that the vortices in clockwise and counter-clockwise directions are neutralized with each other, or that the overall vorticity strengths are extremely weak. On the contrary, when the vorticity is very strong (positive means rotating counter-clockwise, negative means rotating clockwise), it indicates that the flow forms a uniform large-scale vortex, so the vorticity field is nearly in the same direction. After identifying the properties of average vorticity, an overview of vorticity at different crank angles with different intake swirl ratio is summarized in Fig. 6.

Fig. 6 shows that the average vorticity changes with different crank angles and swirl ratio. The negative value means that bulk flow is in a clockwise direction. For most crank angles, a higher swirl ratio increases the absolute value of vorticity. This result is reasonable since a high intake swirl motion introduces a stronger swirl to the in-cylinder flow field. Even among a certain swirl ratio, the average vorticity varies with different crank angles because both valve lift and piston movement affect the in-cylinder flow swirl characteristics. During early intake stroke, vorticity is small because of the structure of multiple small-scale vortices. For the same reason, during this period, the differences in swirl ratio are small, showing insignificant bulk swirl motions. When the intake valve lift profile is overlaid onto the vorticity plot, a clear trend can be observed from the valve starting position to its maximum
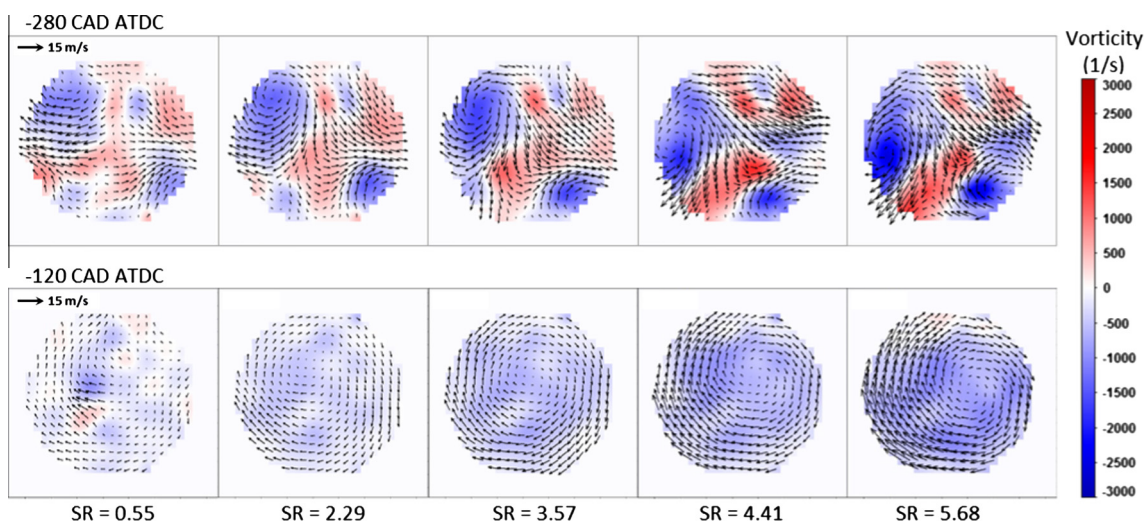

Fig. 5. Ensemble average flow fields of five swirl ratio at −280 CAD and −120 CAD ATDC. Arrows in the figure represent the flow field and the background color indicates the flow vorticity strength (positive value means counter-clockwise rotation, negative value means clockwise). (For interpretation of the references to colour in this figure legend, the reader is referred to the web version of this article.)
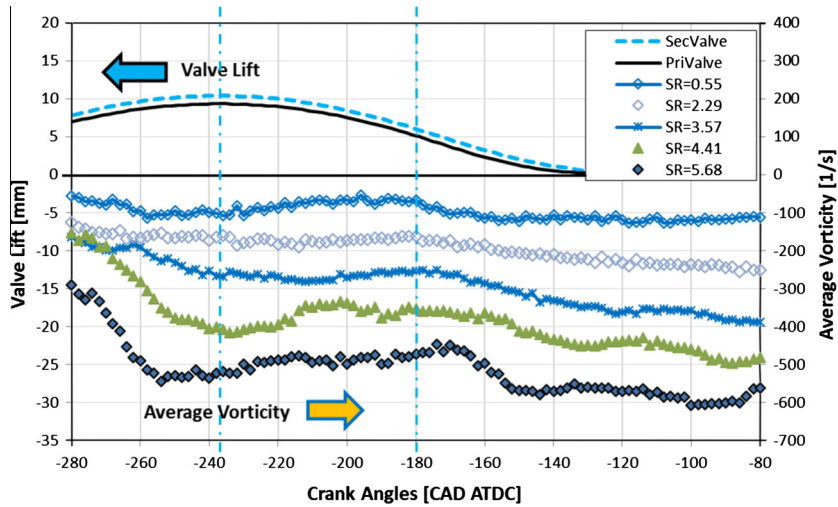
Fig. 6. Average vorticity of five swirl ratio of various crank angles with valve lift overlaid. The left vertical dot-dash line indicates the valve maximum opening position, and the right line locates at the bottom dead center (−180 CAD ATDC).

opening position. When the intake valves are opening from −280 CAD ATDC to −237 CAD ATDC, the average vorticity decreases. The reduction of average vorticity also depends on the magnitude of the swirl ratio. As illustrated in Fig. 6, the largest reduction of vorticity happens when the SR is 5.68. This is because a stronger swirl charge motion generates a faster swirling flow inside the cylinder. The vorticity reaches a plateau after the maximum valve lift point around −237 CAD ATDC. During this period, intake air movement dissipates sufficiently so that only large scale swirl motion remains. Then, after reaching the bottom dead center, the piston begins to move up and squishes the air, causing momentum exchanges within swirl planes and between neighboring planes. These phenomena equalize the swirl motion so that the average vorticity increases gradually below the bottom dead center.

Clear differences can be observed in the average vorticity of various swirl ratio values. If the focus is concentrated on a certain crank angle (for example −200 CAD ATDC), it is possible to determine how average vorticity changes as a function of the swirl ratio. In Fig. 7, the average vorticity of each swirl ratio at −200 CAD ATDC has been plotted in diamond symbols. A well matched linear trend can be observed and a linear regression is also overlaid on the figure. From the physics of swirl motion, a large uniform vortex structure causes a high swirl ratio, but chaotic small-scale vortices diminish the swirl motion causing low swirl ratio. Therefore, it is

reasonable to consider a zero swirl ratio, which corresponds to a zero vorticity. This explains why a linear regression has the form of interception with the origin (0, 0). Based on the linear regression line, the coefficient of determination (R^2), can be obtained to represent the goodness of the data fit with the following expression:

$$R^2 = 1 - \frac{\sum_{i=1}^{n}(ax_i - y_i)^2}{\sum_{i=1}^{n}(y_i - \bar{y})^2}, \tag{11}$$

where $\bar{y} = \frac{1}{n}\sum_{i=1}^{n}y_i$ represents the mean of the observed y_i data (the average vorticity in this situation); x_i is the swirl ratio; a represents the slope of the fit function. A perfect fit can have the coefficient of determination (R^2) approaching unity. In the current example, R^2 is 0.974, which means that this linear regression line can match the original data very well. The strong linearity existing among the average vorticity of different swirl ratios provides convincing evidence of the relationship between vorticity characteristics and swirl ratio.

Further analysis illustrates the strong linearity between the average vorticity and swirl ratio for a wide range of crank angle degrees. The R^2 at each crank angle is shown in Fig. 8, with valve lift profiles overlaid. Since the R^2 is less than 0.9 from −280 CAD ATDC to about −237 CAD ATDC, it does not show a good linear relationship for this period. At this stage, air charge motion is strong and the interactions with valve and cylinder wall are also significant. In order to comprehend the flow field structures in the early intake stroke, as previously illustrated in Fig. 5, the flow structures at −280 CAD ATDC exhibit strong spatial variations. The
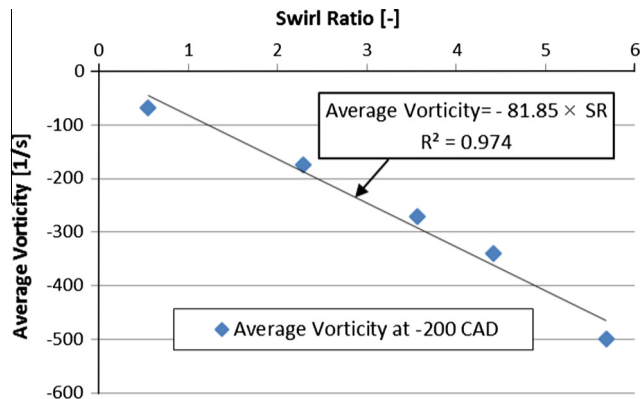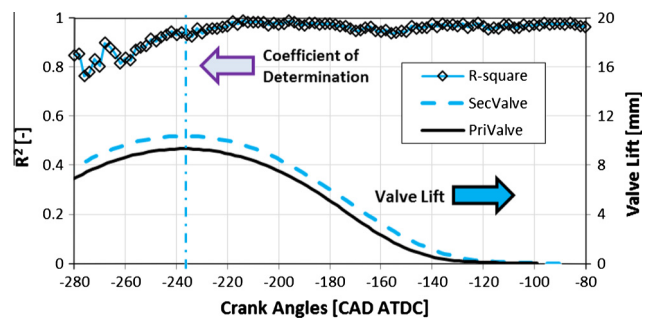

Fig. 7. Linear fit between average vorticity with different swirl ratios at −200 CAD ATDC. Diamonds indicate the average vorticity at different swirl ratio, while the solid line presents the linear regression function.

Fig. 8. R^2 of linear fit between average vorticity with swirl ratio at various crank angles overlaid with valve lifts.
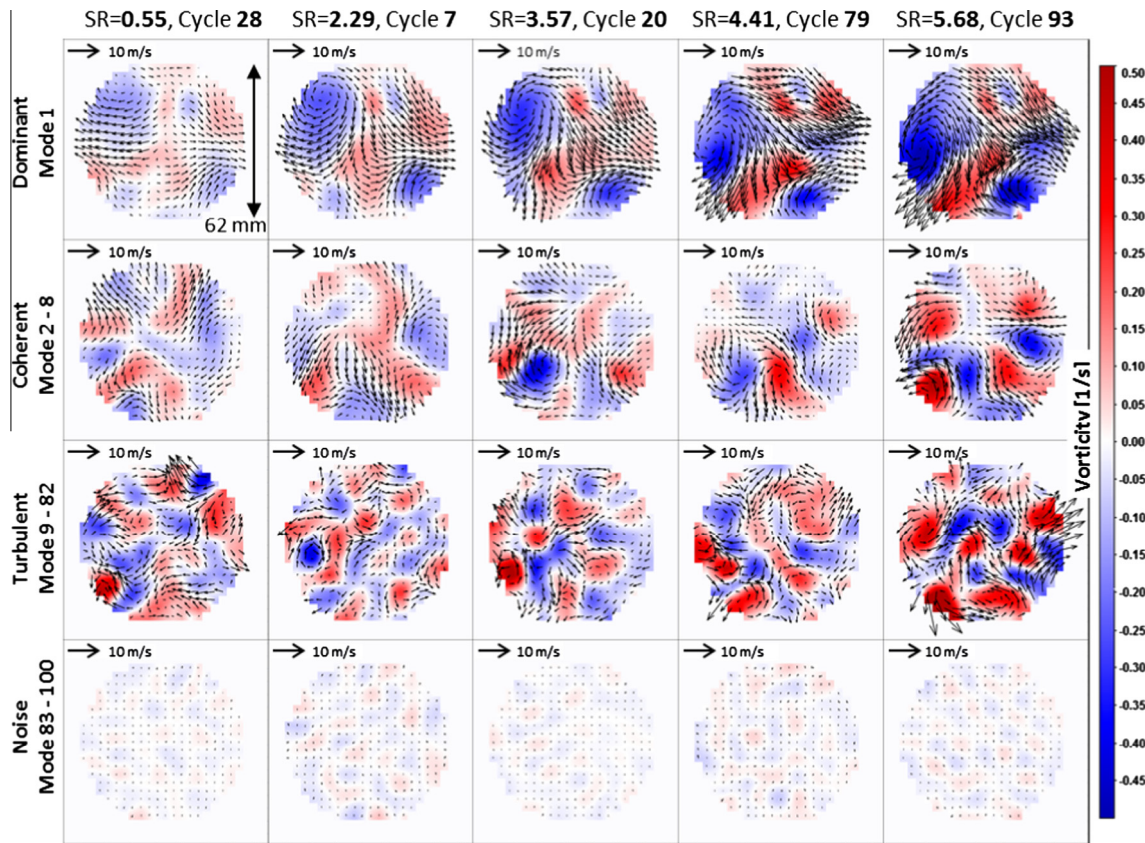
Fig. 9. Reconstructed structures of typically selected cycles at various swirl ratios at −280 CAD ATDC. Arrows in the figure represent the flow field and the background color indicates the flow vorticity strength (positive value means counter-clockwise rotation, negative value means clockwise). (For interpretation of the references to colour in this figure legend, the reader is referred to the web version of this article.)

lack of large swirl structure contributes to the low coefficient of determination in the linear regression line at early intake stage from −280 to −237 CAD. After the maximum valve lift near −237 CAD ATDC, the coefficient of determination increases to approach one. During this period, the flow starts to form large-scale vortex in the cylinder, so the flow characteristics are more similar to the swirl motion structure. This similarity provides a good linearity of vorticity summation and high R^2 value.

The previous section illustrates a novel method for linking the vorticity obtained from PIV experiments to the swirl ratio measured on the cylinder head flow bench by verifying different measurement techniques. While the flow bench measurement of the swirl ratio focuses on macroscopic in-cylinder flow characteristics, the PIV experiment on a single swirl plane provides detailed flow structure information of swirl ratio with considerable accuracy. However, the lack of spatial revolution limits the reliability of this method. It is therefore essential to extend the flow field analysis to a 3D space of the entire cylinder using tomographic-PIV.

The main discussion thus far has focused on correlating the vorticity with swirl ratio. The conclusion of good linearity between them not only provides a potential method for measuring swirl ratio by optical diagnostics, but also verifies the reliability of the swirl ratio used in this study. Based on this conclusion, the results obtained from quadruple POD are more convincing and accurate. According to previous explanation of quadruple POD method (which is at single swirl ratio and single crank angle), efforts have been made to carry out the technique over all the swirl ratio and crank angles; the size of the dataset makes it difficult to display its novelty over classical POD results.

In the next sections, attention is drawn to structures derived by the quadruple POD, as well as trends and variations in kinetic energy captured by each structure. Note that, after reconstruction, the cycle-to-cycle variation properties will be kept for the reconstructed structures. So in the following sections, only the representative individual flow field is used to present the reconstructed flow field, because the ensemble average cannot properly display flow information in this situation.

Fig. 9 depicts the reconstructed structures of selected cycles at five swirl ratio values. The flow field velocity scale is the same and the color indicates the strength of vorticity. A clear similarity can be observed between adjacent swirl ratio values in the dominant structure. This is the most significant flow field characteristic and the increase of swirl ratio enhances the intake air strength. Since one intake port has been partially or fully blocked, the intake air velocity increases in order to maintain the intake runner pressure. The coherent structure also illustrates large scale vortices. The coherent structure is weaker than the dominant structure, but flow structure varies considerably among different swirl ratios. Vorticity strength in the coherent structure increases significantly with increasing intake air swirl ratio. In the turbulent structure, the differences introduced by the swirl ratio are diminished. At each swirl ratio, the turbulent structure shows a highly fluctuating flow field with many small-scale vortices; it exists throughout all the intake swirl ratios. The strength of turbulent areas of flow fields under various swirl ratios are similar. Finally, since the noise structure is quite small compared to other structures, it can usually be ignored during the analysis.

When the engine undergoes the compression stroke, the effect of intake charge motion reduces to a uniform single vortex

structure, as shown in the first row of Fig. 10. At −80 CAD ATDC, the dominant structures have smaller velocity than −280 CAD ATDC, but the swirl directions are identical. The intake valve closes at around −140 CAD ATDC; after that the intake charge motion stops. The air structure interactions with each other, and against the cylinder wall and piston top, leads to a dissipation in kinetic energy. Moreover, these interactions also decrease the coherent flow and turbulent strength comparing to that at −280 CAD, which can be obtained from the second and third rows of Figs. 9 and 10. Compared to Fig. 9, the coherent flow becomes much weaker, but large multiple vortex structures remain. Due to the limitation of single cycle results, this relationship between flow kinetic energy and swirl ratio cannot be drawn from the results in Fig. 10. The turbulent structure behaves similarly when the intake stroke contains large spatial variations in the flow, and the noise structure is still very small.

Due to the cycle-to-cycle variations in engines, single cycle results cannot accurately reflect the characteristics of the overall flow behavior. Therefore, statistical analysis on kinetic energy captured by each reconstructed structure is applied. Kinetic energy is calculated based on the velocity field and it represents the magnitude of flow velocity. The mean kinetic energy of the 100 cycles at each crank angle and swirl ratio indicates the average level of energy while the root mean square (RMS), represents the variations in kinetic energy among the 100 cycles. The RMS calculation is according to Eq. (12):

$$RMS = \sqrt{\frac{1}{N-1}\sum_{i=1}^{N}(x_i - \bar{x})^2}, \qquad (12)$$

where N means the total number of the input cycles, which is 100 in this paper. x_i indicates the kinetic energy of ith cycle and $\bar{x}$ represents the mean value of the kinetic energy of all N cycles.

As seen in Fig. 11, the mean kinetic energy of the dominant structure shows clear differences among various swirl ratios. High intake air swirl ratio contributes to high kinetic energy during intake and compression strokes while the RMS values remain similar to the mean energy. Since the analysis of averaged flow characteristics have been discussed in previous section using the average vorticity calculation, the trend of mean kinetic energy of the dominant flow will not be repeated here. For the RMS values, high swirl introduces higher fluctuations during the air charge motion, so the cycle-to-cycle variations of the kinetic energy is higher than at low swirl condition. However, considering that the mean kinetic energy of highest swirl is four to five times larger than the lowest swirl, the RMS of the highest swirl is only about twice that of the RMS with the lowest swirl. So the coefficient of variation (COV), of the highest swirl is about half that in the lowest swirl. This indicates that high swirl actually helps suppress variations by introducing a directional flow.

The coherent structure shows some differences in the kinetic energy with various swirl ratios during early intake stroke. This difference diminishes with engine motoring to compression stroke. The mean kinetic energy of the coherent structure gradually decreases to a very low level, and the RMS value also decreases. This result is consistent with the observations from the comparison of coherent structure strength depicted in Figs. 9 and 10. The large-scale spatial variation in the flow field is captured by the coherent structure. During intake stroke, intake air charge motion
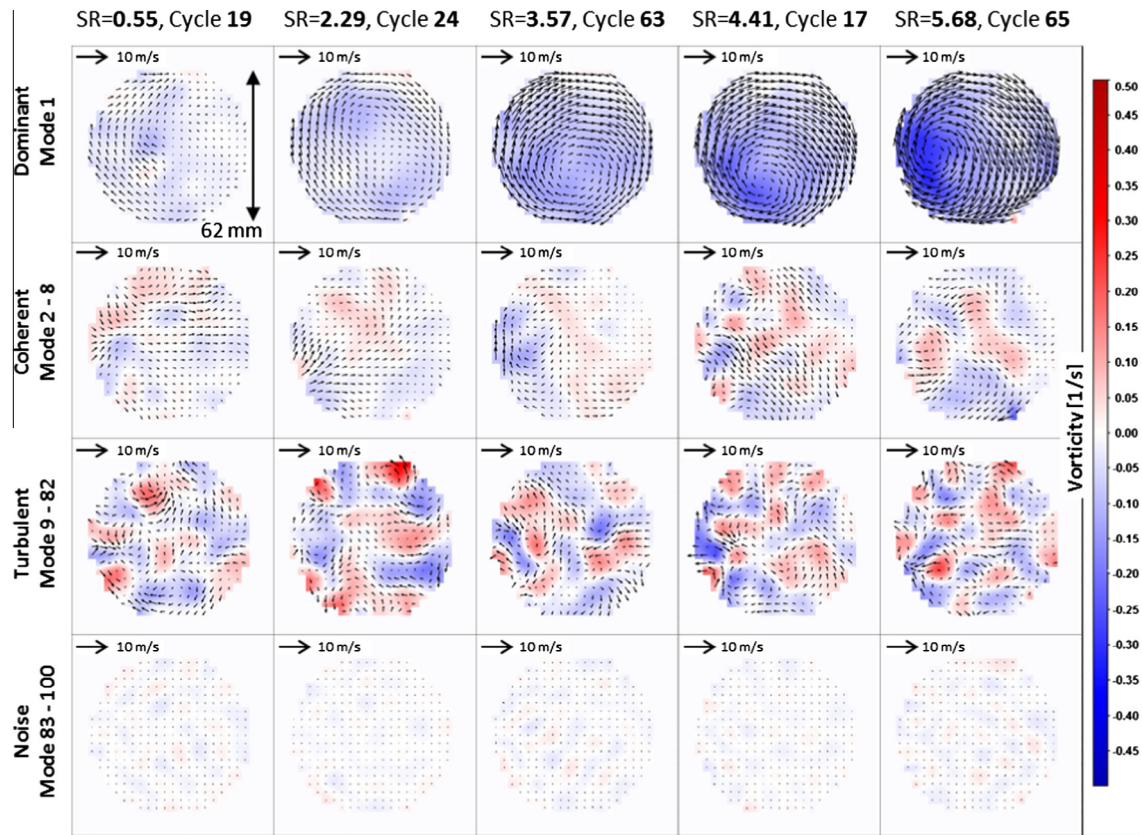

Fig. 10. Reconstructed structures of typically selected cycles at various swirl ratios at −80 CAD ATDC. Arrows in the figure represent the flow field and the background color indicates the flow vorticity strength (positive value means counter-clockwise rotation, negative value means clockwise). (For interpretation of the references to colour in this figure legend, the reader is referred to the web version of this article.)
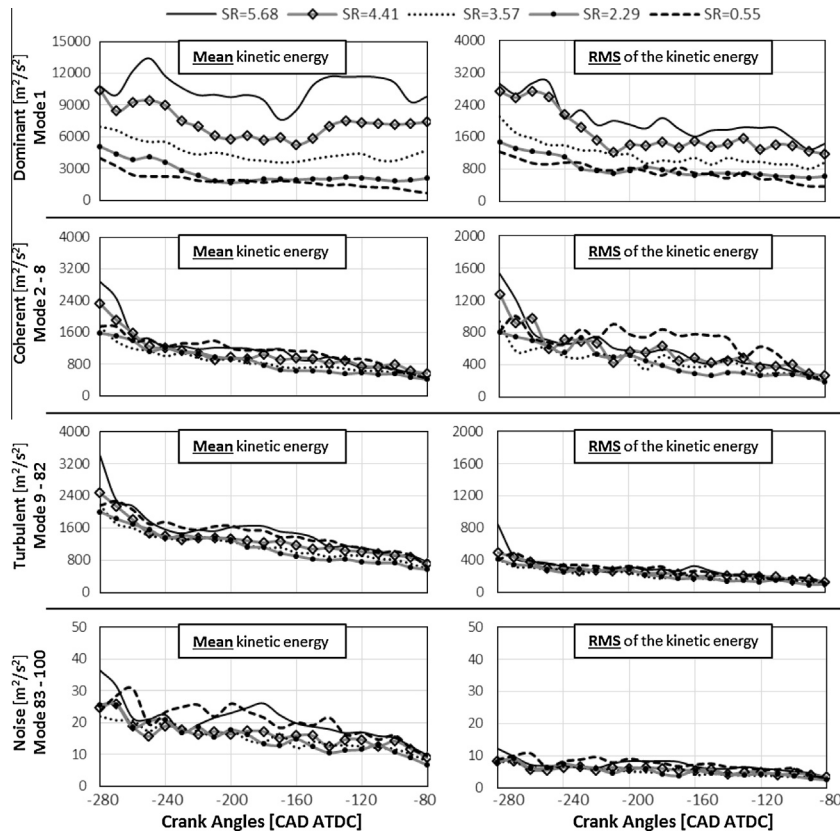
Fig. 11. Mean and RMS of kinetic energy captured by each structure. Note that the y-axis range is different between mean and RMS in first three rows.

is unstable due to valve lifting, air-to-air interaction, and air-to-wall interaction; therefore, the kinetic energy is highest in the beginning, where dissipation has only occurred for a short time. In the late intake and early compression stroke, the large-scale coherent structure at the lowest swirl ratio displays the largest RMS value of kinetic energy. Since the lowest swirl condition introduces low intake charge velocity, the flow velocity dissipation rate is not as fast as that in high swirl condition between late intake and early compression stroke. For this reason, there is high RMS of kinetic energy in the low swirl coherent structure during that period.

The turbulent structure behaves differently from the coherent structure in both mean energy and RMS value; smaller differences can be found between turbulent and coherent structures in the mean kinetic energy. Since large-scale flow characteristics introduced by the intake swirl ratio have been captured by the dominant and coherent structures, the turbulent structure captures the highly fluctuating characteristics of the flow field. The turbulent strength among different swirl ratios remains about the same at various crank angles. The decreasing trend of the mean kinetic energy with crank angle is the same as the coherent structure, due to the dissipation of flow energy through interactions. Compared to the coherent structure, the RMS of kinetic energy of the turbulent structure is very low, which means that the turbulent structure exists as a stable background structure in the cylinder. Therefore the contribution of a turbulent structure to cycle-to-cycle variations is very limited. Finally, since the noise structure only contains very low values of mean and RMS of kinetic energy, it can be regarded as high order fluctuations in the flow field and can therefore be neglected.

5. Summary

A high speed PIV experiment was implemented to measure in-cylinder flow fields at five different intake swirl ratios. A vorticity analysis and quadruple POD technique were applied to analyze the flow characteristics. The average vorticity analysis was used to build the correlation between the ensemble averaged vorticity field and the swirl ratio, while the quadruple POD was applied to study the higher order variation structure characterization and the cycle-to-cycle variation. The following conclusions are drawn:

1. For specific engine and test conditions in this investigation, the average vorticity of the flow field at the focal plane (swirl plane at 30 mm below injector tip) exhibits good linearity when correlated with the intake swirl ratio. This approach verifies the reliability of the quadruple POD approach and provides a potential method for measuring the engine intake swirl ratio by implementation of the PIV test.
2. The average vorticity is strongly affected by the valve motion. The vorticity increases when the valve lift increases until the valve reaches the maximum lift point. Afterwards, the average vorticity increases with a higher intake swirl ratio.
3. The quadruple POD technique classifies individual modes into several categories to reflect more accurate features of flow structure than the classical POD technique. In the classical POD technique, differences between two adjacent modes can be quite small, so the single mode is not capable of capturing the flow property. Using the quadruple POD method allows the differentiation of complex flow structures into dominant structure, coherent structure, turbulent structure, and noise structure.

4. The dominant structure captures the effect of intake swirl ratio while the coherent structure captures the large-scale flow characteristics. Both of these two structures show larger extent of cycle-to-cycle variations. The turbulent structures are stronger than the coherent structure and they have very small cycle-to-cycle variations in the kinetic energy. This indicates strong and consistent turbulent motion during engine intake and compression strokes. For this reason, the turbulent structures are only affected slightly by the intake swirl ratio. Finally, the noise structure can be neglected due to the low energy captured.

This research provides a novel way to study the in-cylinder flow under various intake swirl ratios. The spatial resolutions of PIV experiments should be increased to fully reveal the in-cylinder flow characteristics on other planes. In addition, improvements will be made to the quadruple POD technique by developing more reasonable classification criteria based on the physics of the in-cylinder flow structure.

Acknowledgments

References

[1] Zhao F, Lai MC, Harrington DL. Automotive spark-ignited direct-injection gasoline engines. Progr Energy Combust Sci 1999;25(5):437–562. http://dx.doi.org/10.1016/S0360-1285(99)00004-0.

[2] Sher E, Bar-Kohany T, Rashkovan A. Flash-boiling atomization. Progr Energy Combust Sci 2008;34(4):417–39. http://dx.doi.org/10.1016/j.pecs.2007.05.001.

[3] Xu M, Zhang Y, Zeng W, Zhang G, Zhang M. Flash boiling: easy and better way to generate ideal sprays than the high injection pressure. SAE Int J Fuels Lubr 2013;6(1):137–48. http://dx.doi.org/10.4271/2013-01-1614.

[4] Porpatham E, Ramesh A, Nagalingam B. Effect of swirl on the performance and combustion of a biogas fuelled spark ignition engine. Energy Convers Manage 2013;76:463–71. http://dx.doi.org/10.1016/j.enconman.2013.07.071.

[5] Lee K, Bae C, Kang K. The effects of tumble and swirl flows on flame propagation in a four-valve S.I. engine. Appl Therm Eng 2007;27(11-12):2122–30. http://dx.doi.org/10.1016/j.applthermaleng.2006.11.011.

[6] Mittal M, Hung DLS, Zhu G, Schock H. High-speed flow and combustion visualization to study the effects of charge motion control on fuel spray development and combustion inside a direct-injection spark-ignition engine. SAE Int J Eng 2011;4(1):1469–80. http://dx.doi.org/10.4271/2011-01-1213.

[7] Li Y, Zhao H, Peng Z, Ladommatos N. Analysis of tumble and swirl motions in a four-valve SI engine. SAE Technical Paper, 2001–01-3555; 2001, http://dx.doi.org/10.4271/2001-01-3555.

[8] Semlitsch B, Wang Y, Mihăescu M. Flow effects due to valve and piston motion in an internal combustion engine exhaust port. Energy Convers Manage 2015;96:18–30. http://dx.doi.org/10.1016/j.enconman.2015.02.058.

[9] Semlitsch B, Wang Y, Mihăescu M. Flow effects due to pulsation in an internal combustion engine exhaust port. Energy Convers Manage 2014;86:520–36. http://dx.doi.org/10.1016/j.enconman.2014.06.034.

[10] Reuss DL. Cyclic Variability of Large-Scale Turbulent Structures in Directed and Undirected IC Engine Flows. SAE Technical Paper, 2000–01-0246; 2000. http://dx.doi.org/10.4271/2000-01-0246.

[11] Ceviz MA. Intake plenum volume and its influence on the engine performance, cyclic variability and emissions. Energy Convers Manage 2007;48(3):961–6. http://dx.doi.org/10.1016/j.enconman.2006.08.006.

[12] Müller S, Böhm B, Gleißner M, Grzeszik R, Arndt S, Dreizler A. Flow field measurements in an optically accessible, direct-injection spray-guided internal combustion engine using high-speed PIV. Exp Fluids 2010;48(2):281–90. http://dx.doi.org/10.1007/s00348-009-0742-2.

[13] Lumley JL. The structure of inhomogeneous turbulent flows. Atmos Turb Radio Wave Propagat 1967:166–78. doi: N/A.

[14] Graftieaux L, Michard M, Grosjean N. Combining PIV, POD and vortex identification algorithms for the study of unsteady turbulent swirling flows. Meas Sci Technol 2001;12(9):1422–9. http://dx.doi.org/10.1088/0957-0233/12/9/307.

[15] Bizon K, Continillo G, Leistner K, Mancaruso E, Vaglieco B. POD-based analysis of cycle-to-cycle variations in an optically accessible diesel engine. Proc Combust Inst 2009;32(2):2809–16. http://dx.doi.org/10.1016/j.proci.2008.08.010.

[16] Chen H, Reuss DL, Sick V. Analysis of misfires in a direct injection engine using proper orthogonal decomposition. Exp Fluids 2011;51(4):1139–51. http://dx.doi.org/10.1007/s00348-011-1133-z.

[17] Sick V, Chen H, Abraham PS, Reuss DL, Yang X, Gopalakrishnan V, Xu M, Kuo T-W. Proper-orthogonal decomposition analysis for engine research. In: 9th Congress, Gasoline Direct Injection Engines, Essen, Germany; 2012. p. 1–12.

[18] Chen H, Hung DL, Xu M, Zhong J. Analyzing the cycle-to-cycle variations of pulsing spray characteristics by means of the proper orthogonal decomposition. Atom Sprays 2013;23(7). http://dx.doi.org/10.1615/AtomizSpr.007851.

[19] Liu K, Haworth DC. Development and Assessment of POD for Analysis of Turbulent Flow in Piston Engines. SAE Technical Paper, 2011–01-0830; 2011. http://dx.doi.org/10.4271/2011-01-0830.

[20] Kapitza L, Imberdis O, Bensler H, Willand J, Thévenin D. An experimental analysis of the turbulent structures generated by the intake port of a DISI-engine. Exp Fluids 2010;48(2):265–80. http://dx.doi.org/10.1007/s00348-009-0736-0.

[21] Druault P, Guibert P, Alizon F. Use of proper orthogonal decomposition for time interpolation from PIV data. Exp Fluids 2005;39(6):1009–23. http://dx.doi.org/10.1007/s00348-005-0035-3.

[22] Vu T-T, Guibert P. Proper orthogonal decomposition analysis for cycle-to-cycle variations of engine flow. Effect of a control device in an inlet pipe. Exp Fluids 2012;52(6):1519–32. http://dx.doi.org/10.1007/s00348-012-1268-6.

[23] Zhuang H, Hung DLS, Chen H. Study of time-resolved vortex structure of in-cylinder engine flow fields using proper orthogonal decomposition technique. J Eng Gas Turb Power 2015;137(8):082604. http://dx.doi.org/10.1115/1.4029600.

[24] Qin W, Xie M, Jia M, Wang T, Liu D. Large eddy simulation and proper orthogonal decomposition analysis of turbulent flows in a direct injection spark ignition engine: cyclic variation and effect of valve lift. Sci China Technol Sci 2014;57(3):489–504. http://dx.doi.org/10.1007/s11431-014-5472-x.

[25] Abraham P, Liu K, Haworth D, Reuss D, Sick V. Evaluating large-eddy simulation (LES) and high-speed particle image velocimetry (PIV) with phase-invariant proper orthogonal decomposition (POD). Oil Gas Sci Technol – Rev IFP Energies Nouvelles 2014;69(1):41–59. http://dx.doi.org/10.2516/ogst/2013126.

[26] Chen H, Xu M, Hung DL. Analyzing in-cylinder flow evolution and variations in a spark-ignition direct-injection engine using phase-invariant proper orthogonal decomposition technique. SAE Technical Paper 2014–01-1174; 2014. http://dx.doi.org/10.4271/2014-01-1174.

[27] Cosadia I, Borée J, Dumont P. Coupling time-resolved PIV flow-fields and phase-invariant proper orthogonal decomposition for the description of the parameters space in a transparent Diesel engine. Exp Fluids 2007;43(2–3):357–70. http://dx.doi.org/10.1007/s00348-007-0338-7.

[28] Fogleman M, Lumley J, Rempfer D, Haworth D. Application of the proper orthogonal decomposition to datasets of internal combustion engine flows. J Turb 2004;5(23):1–3. http://dx.doi.org/10.1088/1468-5248/5/1/023.

[29] Roudnitzky S, Druault P, Guibert P. Proper orthogonal decomposition of in-cylinder engine flow into mean component, coherent structures and random Gaussian fluctuations. J Turb 2006;7:N70. http://dx.doi.org/10.1080/14685240600806264.

[30] Qin W, Hung DLS, Xu M. Investigation of the temporal evolution and spatial variation of in-cylinder engine fuel spray characteristics. Energy Convers Manage 2015;98:430–9. http://dx.doi.org/10.1016/j.enconman.2015.03.093.

[31] Chen H, Reuss DL, Sick V. On the use and interpretation of proper orthogonal decomposition of in-cylinder engine flows. Meas Sci Technol 2012;23(8):085302. http://dx.doi.org/10.1088/0957-0233/23/8/085302.

[32] Chen H, Reuss DL, Hung DL, Sick V. A practical guide for using proper orthogonal decomposition in engine research. Int J Eng Res 2012;14(4):307–19. http://dx.doi.org/10.1177/1468087412455748.